

See discussions, stats, and author profiles for this publication at: <https://www.researchgate.net/publication/262180001>

Understanding Copper Activation and Xanthate Adsorption on Sphalerite by Time-of-Flight Secondary Ion Mass Spectrometry, X-ray Photoelectron Spectroscopy, and in Situ Scanning Elec...

ARTICLE *in* THE JOURNAL OF PHYSICAL CHEMISTRY · SEPTEMBER 2013

Impact Factor: 2.78 · DOI: 10.1021/jp407795k

CITATIONS

8

READS

86

3 AUTHORS, INCLUDING:



[Qingxia Liu](#)

University of Alberta

78 PUBLICATIONS 788 CITATIONS

[SEE PROFILE](#)



[Hongbo Zeng](#)

University of Alberta

135 PUBLICATIONS 1,935 CITATIONS

[SEE PROFILE](#)

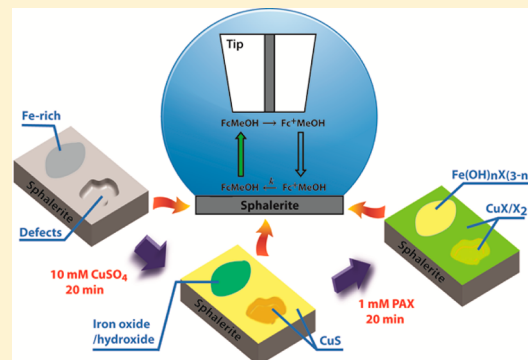
Understanding Copper Activation and Xanthate Adsorption on Sphalerite by Time-of-Flight Secondary Ion Mass Spectrometry, X-ray Photoelectron Spectroscopy, and in Situ Scanning Electrochemical Microscopy

Jingyi Wang, Qingxia Liu, and Hongbo Zeng*

Department of Chemical and Materials Engineering, University of Alberta, Edmonton, Alberta, T6G 2V4, Canada

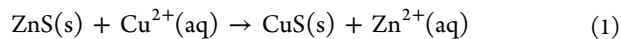
S Supporting Information

ABSTRACT: In situ scanning electrochemical microscopy (SECM) was applied for the first time to study the copper activation and subsequent xanthate adsorption on sphalerite. The corresponding surface compositions were analyzed by time-of-flight secondary ion mass spectrometry (ToF-SIMS) and X-ray photoelectron spectroscopy (XPS). The probe approach curve (PAC) using SECM shows that unactivated and activated sphalerite surfaces have negative current feedback and partially positive current feedback, respectively, suggesting that Cu_xS is formed on the sphalerite after copper activation. The copper activation of sphalerite strongly depends on the surface heterogeneity (e.g., presence of polishing defects, chemical composition), impacting the subsequent xanthate adsorption process. The SECM, ToF-SIMS, and XPS analyses show that during the copper activation the polishing defects, which have high excess surface energy, tend to consume more copper ions, resulting in Cu-rich regions by forming CuS-like species, while Fe oxide/hydroxide forms at Fe-rich regions. The XPS spectra further confirm that the CuS-like species involve Cu(I) and S(–I). The SECM imaging shows that after xanthate adsorption the current response at the Cu-rich regions decreases because of the formation of cuprous xanthate (CuX) and dixanthogen (X₂) while increases at the Fe-rich regions mainly due to the chemisorption of xanthate on Fe oxide/hydroxide. Our results shed light on the fundamental understanding of the electrochemical processes on sphalerite surface associated with its copper activation and subsequent xanthate adsorption in flotation.



1. INTRODUCTION

Sphalerite (zinc sulfide mineral) is the most important source of zinc metal, which is bioabsorbable¹ and known as an essential trace element for life and has many industrial uses such as protective coatings for steel. Zinc sulfide has many applications such as lubricant additives,² luminescent materials,³ and pigments.⁴ Flotation has been widely applied by industry to separate and concentrate valuable minerals from gangue.^{5–7} One critical procedure in sphalerite flotation is to increase the surface hydrophobicity of sphalerite to allow the attachment of air bubbles in a water–ore pulp, in which short-chain thiols, such as xanthate, are normally used as so-called collectors. However, the attachment of xanthate to sphalerite surface is weak because they form a zinc–xanthate compound, which has a high solubility in water.^{7,8} Additional chemicals, so-called activators, are generally added to treat the mineral surfaces to enhance the adsorption of collector molecules. Copper sulfate (CuSO₄) is the most commonly used activator in sphalerite flotation, and the copper activation of sphalerite follows an ion exchange mechanism as widely accepted and shown in eq 1.^{6–8}



Much effort and significant progress has been made since the 1920s on copper activation and xanthate adsorption in sphalerite flotation, most of which focused on the effects of surface oxidation,^{9–11} concentration of activators and collectors,^{11–13} conditioning time,^{14,15} solution pH,^{13,15,16} and iron (an impurity within natural sphalerite).^{10,17–19} Despite the significant progress achieved, the understanding of the surface reaction mechanisms and products associated with the activation and flotation of sphalerite still remains limited. Some of the results reported were even controversial,²⁰ particularly on the effect of iron present in the sphalerite lattice on the copper activation and collector adsorption. Iron is a major impurity in sphalerite, which decreases the band gap of sphalerite and consequently affects its reactivity. It was reported by Gigowski et al.¹⁰ that iron-rich sphalerite tends to adsorb more copper ions during flotation, which is beneficial to the activation and subsequent xanthate adsorption processes. Later, Patrick et al.¹⁷ applied the reflection extended X-ray absorption

Received: August 4, 2013

Revised: September 4, 2013

Published: September 6, 2013

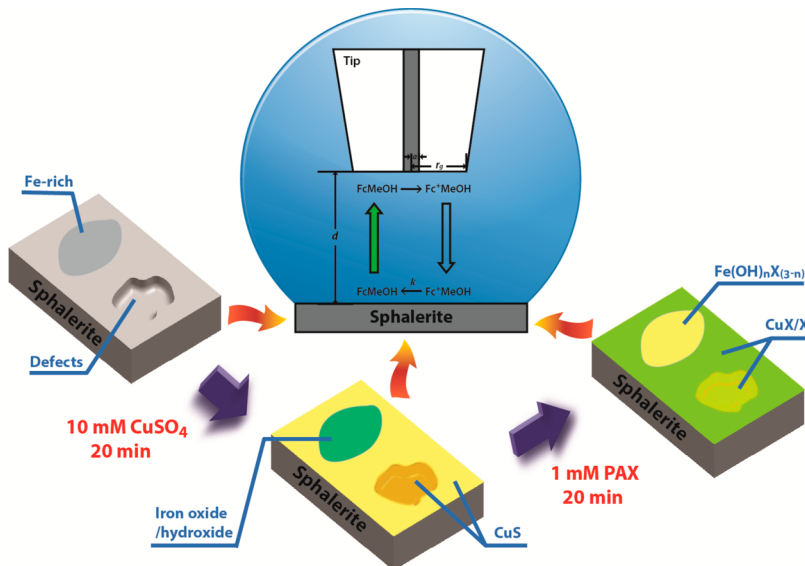


Figure 1. Schematic of the in situ imaging of copper activation and xanthate adsorption on sphalerite using SECM under feedback mode.

fine structure (REFLEXAFS) technique to obtain the structural information on sphalerite surfaces and revealed that the iron on sphalerite surface is bonded to oxygen which can inhibit the initial copper activation but appears to facilitate the formation of covellite on xanthate addition. However, previous flotation experiments showed that the presence of iron in sphalerite is detrimental to its recovery, which reduces the copper activation of sphalerite and therefore leads to a reduction in collector adsorption.¹⁸ Nevertheless, recent atomic force microscopy (AFM) imaging showed that the higher the bulk iron content in sphalerite, the larger the number of cleavage steps and the larger the precipitate size of oxidation products during the copper activation, which implies that iron enhances the copper activation rate.¹⁹ Furthermore, the X-ray photoelectron spectroscopy (XPS) analysis indicates an increased copper concentration and the formation of disulfide and polysulfide that correlates with an increase in bulk iron content.¹⁹ It should be noted that in the above studies, the experimental conditions, such as pretreatment, pH of solutions, and conditioning time, were very different. The iron distribution in sphalerite is normally inhomogeneous at the microscale.²¹ Consequently, it is difficult to draw a general conclusion about the impact of iron on sphalerite flotation based on the previous studies. Therefore, it is of fundamental and practical importance to understand the interfacial phenomena occurring at the iron-rich and iron-poor phases on sphalerite surfaces at the microscale during the copper activation and xanthate adsorption.

Secondary ion mass spectrometry (SIMS) is a very sensitive technique for analyzing and mapping the chemical composition of solid surfaces and thin films, and it has been successfully applied to investigate the type and distribution of chemical species on sphalerite surface.^{22–29} For example, Boulton et al. proposed a flotation mechanism of sphalerite and pyrite in a mixed mineral system by characterizing the distribution of chemical species on mineral surfaces through time-of-flight secondary ion mass spectrometry (ToF-SIMS).²⁶ ToF-SIMS is more surface-sensitive than X-ray photoelectron spectroscopy (XPS) and enables submonolayer analysis with parts-per-million sensitivity. However, ToF-SIMS may cause certain degrees of surface damages of the sample during the analysis.³⁰ In order to monitor the transformation of surface species on

the sphalerite surface during the copper activation and the subsequent xanthate adsorption, in addition to ToF-SIMS and XPS studies, in situ and nondestructive measurements are expected to provide important complementary information. One of the suitable techniques for such measurements is scanning electrochemical microscopy (SECM).

SECM is a scanning probe microscopy, and the principal of SECM is based on faradaic current changes as a small ultramicroelectrode (UME) tip is moved across a substrate in solutions, which enables the in situ probing of surface reactivity of the substrate.^{31–35} In a recent report by Chen et al., SECM and cyclic voltammetry (CV) were employed to probe the copper sulfide (Cu_xS) microstructures deposited on Si(111) wafers that showed that the Cu_xS film had good electrical conductivity with an apparent electron-transfer rate constant (k) of 0.04 cm/s.³⁶ Another advantage of SECM is that no electrical connection is needed between the sample substrate and an external circuit,³² as required in traditional electroanalytical techniques. Consequently, SECM is suitable for the studies of less conductive or insulating substrates, such as sphalerite, which has a large band gap of 3.7 eV.³⁷

In this work, SECM was employed, for the first time, to probe the surface reactivity of sphalerite before and after copper activation and xanthate adsorption in situ. The surface composition was further analyzed by ToF-SIMS and XPS. The investigation by employing a combination of SECM, ToF-SIMS, and XPS techniques provides new insights into the iron effect on the copper activation and subsequent xanthate adsorption associated with sphalerite flotation.

2. MATERIALS AND EXPERIMENTAL METHODS

2.1. Materials. Cupric sulfate pentahydrate ($\text{CuSO}_4 \cdot 5\text{H}_2\text{O}$, ACS reagent grade, Fisher Scientific), potassium amyl xanthate ($\text{C}_6\text{H}_{11}\text{OS}_2\text{K}$, Prospec Chemicals Ltd., Canada), ferrocenemethanol (FcMeOH , 97%, Acros Organics), potassium nitrate (KNO_3 , ACS reagent grade, MP Biomedicals, LLC), sodium chloride (NaCl , ACS certified, Fisher Scientific), sodium hydroxide (NaOH , ACS certified, Fisher Scientific), ferrous chloride tetrahydrate ($\text{FeCl}_2 \cdot 4\text{H}_2\text{O}$, ACS certified, Fisher Scientific), and carbon paste oil base (ALS Co., Ltd., Japan) were used as received. All aqueous solutions were prepared

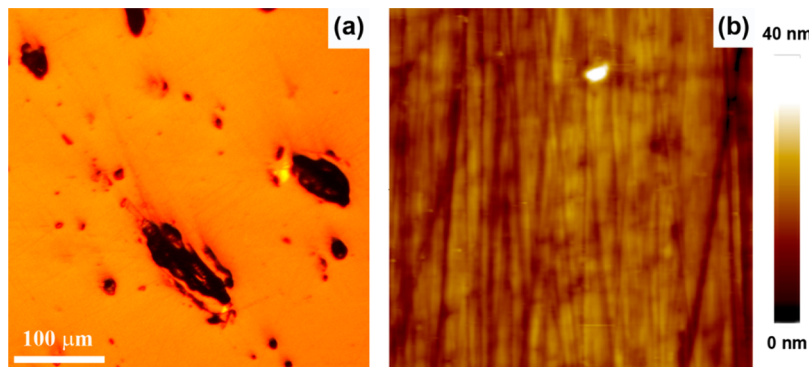


Figure 2. (a) Optical microscope image of freshly polished sphalerite; (b) a typical AFM topography image of the bright regions in (a) with a surface roughness R_q of 2.1 nm (image size $5 \times 5 \mu\text{m}^2$).

using Milli-Q water (Millipore deionized, 18.2 $\text{M}\Omega\cdot\text{cm}$ resistivity). Potassium amyl xanthate (PAX) was purified by adding 100 g of xanthate into 1000 mL of warm acetone at 40 °C on a water bath, stirring for a few minutes, and precipitated by ether following an established method.^{38,39}

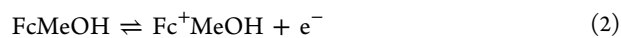
2.2. Preparation of Sphalerite Samples. Sphalerite (Crystalline, Ward's Natural Science) were crushed, polished by hand with wet silicon carbide paper in the sequence of 60, 240, 320, 400, 600, 800, 1200 grit, and then polished with 5 and 1 μm alumina powder suspensions, respectively. The freshly polished sphalerite samples were ultrasonically washed in Milli-Q water, ethanol, and Milli-Q water for 5 min respectively. The cleaned sphalerite samples were dried by highly pure N_2 . The freshly prepared sphalerite samples were immediately transferred into the electrochemical cell for SECM experiments.

2.3. Surface Characterization. The selected areas of freshly polished sphalerite were observed using a metallurgical optical microscope. An atomic force microscope (AFM) was used to image and determine the roughness of freshly polished sphalerite surfaces. The surface iron concentration of freshly polished sphalerite was estimated by energy dispersive X-ray analysis (EDX) on a Hitachi S-2700 scanning electron microscope equipped with a Princeton Gamma-Tech IMIX digital imaging system and a PGT PRISM IG (intrinsic germanium) detector. The ToF-SIMS composition mapping was conducted on an ION-TOF ToF-SIMS IV (ION-TOF, Munster, Germany) equipped with a bismuth liquid ion source. The XPS spectra were obtained on an AXIS 165 spectrometer (Kratos Analytical). The binding energy 284.6 eV of C 1s was used as a reference.

2.4. SECM Measurements. The SECM experiments were performed on a CHI920c scanning electrochemical microscope (CH Instruments, Austin, TX). A Pt ultramicroelectrode (UME) with radius $a = 5 \mu\text{m}$ and $\text{RG} \approx 10$ ($\text{RG} = r_g/a$; r_g is the radius of glass sheath) was used as an SECM tip as shown in Figure 1. The tip was polished on a micropolishing cloth with 0.05 μm alumina powder suspension and rinsed thoroughly with ethanol and Milli-Q water before use. A freshly prepared sphalerite sample was mounted at the bottom of a SECM cell with an exposed geometric surface area of $\sim 0.28 \text{ cm}^2$ to the electrolyte solution. A Pt wire was used as a counter electrode, and an Ag/AgCl (1 M KCl) electrode was used as a reference electrode (0.236 V vs SHE). All potentials quoted in this work were referred to this reference electrode unless otherwise specified.

A 1 mM FcMeOH solution was introduced into the SECM cell with 0.1 KNO_3 as the supporting electrolyte. The Pt tip was

biased to a potential of 0.50 V to ensure that the electrooxidation of FcMeOH (eq 2) was under diffusion control when the tip–substrate separation distance d was large enough.³²



The tip current $i_{T,\infty}$ can be described by eq 3,³²

$$i_{T,\infty} = 4nFDa(C_0) \quad (3)$$

where n is the number of transferred electrons, F the Faraday constant, D the diffusion coefficient, a the tip radius, and C_0 the bulk concentration of reactant. The sphalerite substrate was left at its open circuit potential. The SECM experiments were performed under the feedback mode, in which the tip current was affected by the chemical nature of substrate as the tip approached the substrate in the solution. The tip current i_T depends on the apparent rate constant k of the regeneration reaction of redox mediator at the substrate (eq 4 and Figure 1). When the UME tip approaches an insulating and inert substrate surface, the substrate hinders the diffusion of the redox mediator (i.e., FcMeOH) toward the tip ($k \rightarrow 0$) and i_T decreases, which is the so-called negative current feedback. A positive current feedback is observed when the UME approaches a more conductive and reactive substrate surface.⁴⁰



The Pt tip was first positioned at $\sim 7 \mu\text{m}$ above the substrate by recording a probe approach curve (PAC). Then the SECM imaging was conducted under amperometry mode (or called constant height mode). The SECM tip was returned to its original position on the substrate after each image was taken, which facilitated the *in situ* investigation of sphalerite surface before and after copper activation and xanthate adsorption. All SECM experiments were conducted at room temperature of 25 °C.

3. RESULTS AND DISCUSSION

3.1. Characterization of Unactivated Sphalerite Surface. Figure 2a shows the optical microscope image of a freshly polished sphalerite surface. The dark regions are polishing defects (pits), which cannot be totally avoided because sphalerite pits easily.⁴¹ A typical AFM topography image of the bright regions is shown in Figure 2b. The surface roughness R_q of the $5 \times 5 \mu\text{m}^2$ area is 2.1 nm. The surface iron concentration of freshly polished sphalerite is around 0.6% in atomic ratio determined by EDX.

Figure 3 shows the typical PACs on unactivated sphalerite surface (red circles) and activated sphalerite surface (blue triangles) superposed with simulated PACs of different apparent rate constant k values and with PACs of insulator (negative feedback) and conductor (positive feedback).

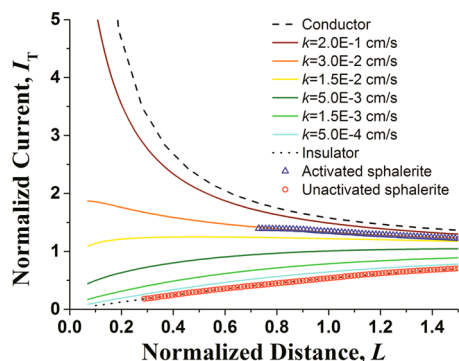


Figure 3. Probe approach curves (PACs) for SECM tip toward unactivated sphalerite substrate (red circles) and activated sphalerite (blue triangles) superposed with simulated PACs of different apparent rate constant k values and with PACs of insulator (negative feedback) and conductor (positive feedback).

triangles), which are superposed with simulated PACs of different k values derived from the theoretical model for a quasi-reversible reaction³⁵ on a substrate of infinite size and with PACs of insulator (negative feedback) and conductor (positive feedback).⁴² For simulated PACs, the normalized current I_T ($i_T/i_{T,\infty}$) and normalized tip–substrate separation L ($L = d/a$) can be correlated by eqs 5–9,

$$I_T = I_S \left(1 - \frac{I_T^{\text{ins}}}{I_T^c} \right) + I_T^{\text{ins}} \quad (5)$$

$$I_T^{\text{ins}} = \frac{1}{0.15 + \frac{1.5358}{L} + 0.58 \exp\left(\frac{-1.14}{L}\right) + 0.0908 \exp\left(\frac{L-6.3}{1.017L}\right)} \quad (6)$$

$$I_T^c = \frac{0.78377}{L} + 0.3315 \exp\left(\frac{-1.0672}{L}\right) + 0.68 \quad (7)$$

$$I_S = \frac{0.78377}{L + \frac{1}{\kappa}} + \frac{0.68 + 0.3315 \exp\left(\frac{-1.0672}{L}\right)}{1 + F(L, \kappa)} \quad (8)$$

$$F(L, \kappa) = \frac{\left(\frac{11}{\kappa L}\right) + 7.3}{110 - 40L} \quad (9)$$

where I_S is the substrate current, I_T^{ins} and I_T^c are the normalized tip currents for insulating substrate and diffusion-controlled regeneration of a redox mediator respectively, and $\kappa = ka/D$. Equations 5–9 are valid in the range $0.1 \leq L \leq 1.5$ and $0.01 \leq \kappa \leq 1000$.³⁵ When typical values from experiments, $I_{T,\infty} = 1.44 \times 10^{-9}$ A (steady state current at Pt tip), $n = 1$, $F = 96\,500$ C, $a = 5 \times 10^{-4}$ cm, and $C_0 = 10^{-3}$ mol L⁻¹, are inputted into eq 3, the diffusion coefficient of FcMeOH is calculated to be 7.46×10^{-6} cm² s⁻¹, which agrees well with the literature value.⁴³ As $k = \kappa D/a$, the above theoretical model is valid in the range 1.492×10^{-4} cm s⁻¹ $\leq k \leq 14.92$ cm s⁻¹.³⁵ Figure 3 shows that the typical experimental PAC curves of unactivated sphalerite (red circles) and activated sphalerite surface (blue triangles) are overlapped with the theoretical prediction for substrates with negative feedback⁴² and partially positive feedback³⁵ (further discussed in section 3.3), respectively, as shown in Figure 3. The various k values were selected so that the simulated PACs shown in Figure 3 cover the transition from insulator case to conductor case. The simulated PACs show that the normalized current I_T increases with increasing the k value, resulting in a transition from negative or partially negative feedback (viz., low conductivity of unactivated sphalerite surface) to partially positive feedback (viz., relatively higher conductivity of activated sphalerite surface) in SECM measurements.

3.2. Nonuniform Copper Activation and Xanthate Adsorption.

Figure 4 shows the SECM images ($400 \times 400 \mu\text{m}^2$) for the same location on sphalerite surface as shown in Figure 2 before the copper activation (Figure 4a), after copper activation (Figure 4b), and after subsequent adsorption of PAX (Figure 4c). As shown in Figure 4a, the areas with relatively higher current response correspond to the polishing defects visible in the microscope image in Figure 2, which was mainly due to the higher reactant flows toward the scanning tip in these areas during SECM imaging in the amperometric

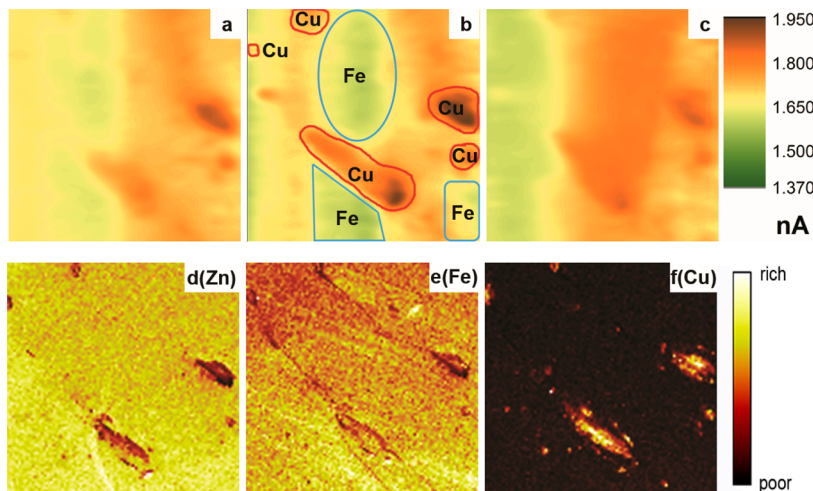


Figure 4. SECM images of a $400 \times 400 \mu\text{m}^2$ area of sphalerite (a) before activation, (b) after activation, and (c) after PAX adsorption. The corresponding SIMS images of (d) Zn, (e) Fe, and (f) Cu after the SECM experiments.

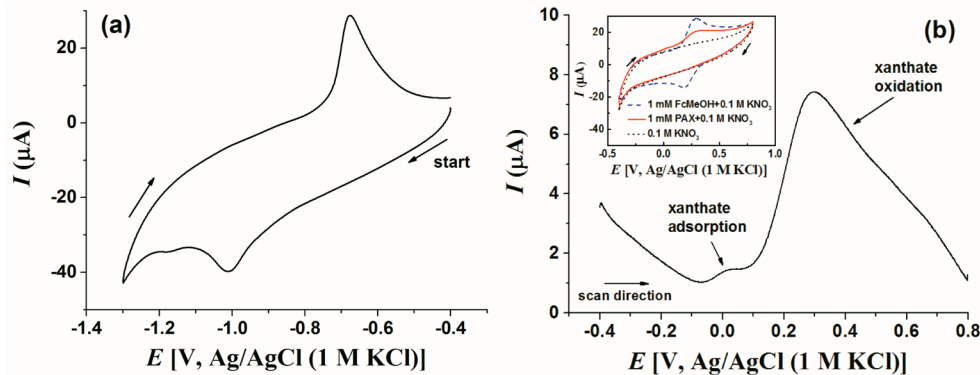


Figure 5. (a) CV curve of CP- Fe_xO_y electrode in 0.1 M NaOH, with a potential sweep rate of 0.02 V s⁻¹. (b) CV curve (positive sweep direction) of CP- Fe_xO_y electrode in 1 mM PAX and 0.1 M KNO₃ after subtraction of the CV curve obtained in 0.1 M KNO₃. Inset shows the CV curves of CP- Fe_xO_y in 0.1 M KNO₃ (black dotted line), in 1 mM PAX and 0.1 M KNO₃ (red solid line), and in 1 mM FcMeOH and 0.1 M KNO₃ (blue dashed line), with a potential sweep rate of 0.1 V s⁻¹.

feedback mode. After the SECM imaging of the freshly polished (unactivated) sphalerite, the cell was rinsed thoroughly with Milli-Q water, and the feed solution was switched to 10 mM CuSO₄ with pH 5.1. The sphalerite substrate was kept immersed in the CuSO₄ solution for 20 min, and the cell was rinsed thoroughly with Milli-Q water and refilled with 1 mM FcMeOH and 0.1 M KNO₃ solution. It is noted that the sphalerite substrate and the SECM probe was fixed during the above process to allow the *in situ* monitoring of the substrate after the treatment with CuSO₄ solution, and the corresponding SECM image is shown in Figure 4b. By comparison of Figure 4a and Figure 4b, it is clear that after the Cu²⁺ treatment, the current responses of certain areas on the activated sphalerite were modified. For example, the current response increased around the polishing defects in Figure 4a and Figure 2, as highlighted by red curves, while it decreased around some other areas as highlighted by blue curves. The current response changes are more visible by subtracting Figure 4a from Figure 4b and subtracting Figure 4b from Figure 4c, as shown in Figure S1a and Figure S1b in the Supporting Information. It should be noted that although in the feedback mode of SECM the current signal in the SECM image depends on both the topography and reactivity of the substrate surface, the current response changes observed in Figure 4 are due to the changes of surface chemistry of the substrate, as the SECM measurements were conducted *in situ* and the tip–substrate distances remained unchanged for the same positions on the SECM images. The different probe approach curves obtained on unactivated and activated sphalerite substrates in Figure 3 also confirm that the current response changes observed in SECM images are due to the surface chemistry changes. The higher current response indicates a larger k value (viz. more active), which could be due to the formation of Cu_xS with a band gap of 2.1 eV and semimetallic conductivity around these areas after the copper activation.³⁶ The above nonuniform change of current response was mainly due to the nonuniform activation of the sphalerite surface, indicating that surface heterogeneity plays an important role in the activation of sphalerite.

After the SECM imaging of copper activated sphalerite surface, a similar procedure was conducted to allow the adsorption of PAX onto the activated sphalerite in 1 mM PAX with a natural pH of 8.3 for 20 min. The cell was then rinsed thoroughly with Milli-Q water and refilled with 1 mM FcMeOH and 0.1 M KNO₃ solution for SECM imaging, as

shown in Figure 4c. Interestingly, the higher current response areas in Figure 4b show lower current response in Figure 4c, while the lower current response areas in Figures 4b show higher current response. The current response change of the sphalerite surface before and after PAX adsorption is strongly dependent on the surface reaction and species formed during the copper activation. It is noted that the SECM technique belongs to the family of scanning probe microscopy, and the lateral resolution is dependent on the UME tip size. In this work, the Pt UME tip has a radius of 5 μm which provides micrometer lateral resolution. A smaller UME tip (e.g., submicrometer or even tens of nanometers) can provide higher lateral resolution.

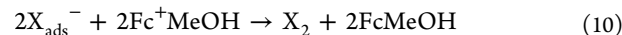
To better interpret the SECM results, SIMS and XPS analyses were conducted after the SECM experiments on the same areas of sphalerite. As the activated sphalerite surface was covered by several layers of PAX,⁴⁴ no signals assigned for the surface element distribution of sphalerite could be detected by SIMS. Therefore, before SIMS analysis, the surface was sputtered by argon to remove the carbon species such as PAX from the surface, and the SIMS images were then recorded. The distributions of Zn, Fe, and Cu are shown in Figure 4d, Figure 4e, and Figure 4f, respectively. It is noted that the high signal intensity of iron is mainly because iron has approximately 10 times higher ion yield relative to zinc.²² The SIMS images clearly show that the polishing defects are Cu-rich but Zn-poor and Fe-poor, which indicates that Cu preferentially adsorbs to these regions. Previous studies showed that polishing defects normally have high excess surface energy where surface reactions (i.e., adsorption and dissolution) will be initiated.^{45–48} The surface reaction rate at the polishing defects is normally higher than that of other regions,⁴⁸ which results in the Cu-rich areas associated with the reaction shown in eq 1. Figure 4b and Figure 4f (Cu distribution) show that the Cu-rich areas correspond to the regions with enhanced current response, suggesting the formation of more conductive species such as Cu_xS.³⁶ Figure 4b and Figure 4e (Fe distribution) reveal that the areas with decreased current response after the copper activation are Fe-rich regions. It has been reported previously that Fe oxyhydroxides appear on the mineral surface after the iron-contained sphalerite is treated in CuSO₄ at pH 5.¹⁹ Therefore, Fe oxide/hydroxide could be present at the Fe-rich regions after the activation of sphalerite in 10 mM CuSO₄ (pH 5.1), resulting in a lower apparent rate constant k of FcMeOH

regeneration reaction. Interestingly, Figure 4b and Figure 4c show that after the sample was treated in 1 mM PAX (pH 8.3) the current response of the Fe-rich regions turns higher while it becomes lower over the Fe-poor regions. It was reported that the xanthate adsorption on chalcopyrite (CuFeS_2) significantly reduces its surface conductivity⁴⁹ because of the formation of cuprous xanthate (CuX) and dixanthogen (X_2).⁵⁰ Similarly, in Figure 4 the current decrease at the Fe-poor regions after PAX adsorption should be attributed to the formation of CuX and X_2 ,^{12,44} which lowers the conductivity of Fe-poor regions. The current increase at the Fe-rich regions after the adsorption of PAX may be due to the chemisorbed xanthate X_{ads}^- on Fe oxyhydroxide to form ferric hydroxyl xanthate, $\text{Fe}(\text{OH})_n(\text{X})_{3-n}$ which is stable above pH 3.5^{51–53} but more oxidizable than CuX (by comparing the Eh-pH diagrams).^{52,54,55} The chemisorbed xanthate can be further oxidized to dixanthogen. Thus, it is likely that some of the chemisorbed xanthate at the Fe-rich regions could get oxidized during SECM imaging.

In order to further verify the proposed mechanism above and the behavior of xanthate at iron oxide/hydroxide surface, iron was electrodeposited on a carbon paste electrode with a diameter of 3 mm in 5 mM FeCl_2 and 0.5 M NaCl solution (pH 5) at -1.15 V for 10 s according to the method reported.⁵⁶ The carbon paste electrode was first polished on weighing paper and cleaned by ethanol and Milli-Q water. After the deposition, iron oxide/hydroxide formation could be achieved on the iron surface even at low pH as reported by Drazic.⁵⁷ The CV curve of iron modified carbon paste electrode in Figure 5a shows a diminished conductivity, which is similar to the CV curves of iron and iron oxide electrode in alkaline solution.^{58–60} The first cathodic peak at -1.01 V during the negative potential sweep is assigned to the reduction of Fe(III) oxide/hydroxide on the iron surface after electrodeposition. The second cathodic peak at -1.17 V is due to the further reduction of iron oxide/hydroxide to iron metal. During the reversal potential sweep, an oxidation peak of Fe(II) oxide/hydroxide at -0.68 V appears corresponding to the formation of a passive oxide layer on the iron surface. The potential sweep stopped at -0.4 V , where the oxidation of Fe(II) oxide/hydroxide was not complete. Therefore, the species on the iron surface should be Fe(II) and Fe(III) oxide/hydroxide, and the resulting electrode is denoted as $\text{CP-Fe}_x\text{O}_y$.

The inset of Figure 5b shows the CV curves of $\text{CP-Fe}_x\text{O}_y$ in blank 0.1 M KNO_3 (black dotted line) in the presence of 1 mM PAX (red solid line) and in the presence of 1 mM FcMeOH (blue dashed line). In 0.1 M KNO_3 , the $\text{CP-Fe}_x\text{O}_y$ only shows the charge-discharge current in the potential range of -0.4 to 0.8 V . When FcMeOH is introduced into the solution, an oxidation peak and a reduction peak can be seen on the CV curve corresponding to the forward and backward reactions of eq 2, respectively. In the presence of PAX, two oxidation peaks appear at about 0 and 0.3 V . By subtraction of the charging current from the total current (sum of the charging current and faradic current), the faradic current peaks can be identified clearly as shown in Figure 5b.⁶¹ The oxidation peak at 0 V is due to the chemisorption of xanthate on $\text{CP-Fe}_x\text{O}_y$ (stage 1), while the oxidation peak at 0.3 V is because of the oxidation of xanthate to dixanthogen (stage 2). A similar two-stage electrochemical reaction was reported for the case of xanthate on pyrite by Li et al.,⁶² and iron oxide/hydroxide was the dominant surface composition under their experimental conditions.⁵² Because the potential for Fc^+MeOH reduction falls in the potential range for the oxidation of chemisorbed

xanthate on $\text{CP-Fe}_x\text{O}_y$ as shown in Figure 5b, the chemisorbed xanthate on the Fe-rich regions could be oxidized by Fc^+MeOH diffused from the Pt tip (eq 4), and the reaction shown in eq 10 could occur. As a result, a current increase was observed at Fe-rich regions after the xanthate adsorption in the SECM measurement of sphalerite. It should be noted that the areas other than the polishing defects also consume copper ions (as long as zinc atoms exist). However, no significant copper signal could be observed at these areas in Figure 4f, which was mainly because the amount of copper–xanthate at these areas was much less than that at the polishing defects and the argon sputtering could remove copper–xanthate from the surface.



3.3. Characterization of Surface Species on Sphalerite after Copper Activation. To better characterize the surface composition of sphalerite after copper activation, a $100 \times 100 \mu\text{m}^2$ region was examined by both SECM imaging and SIMS mapping before and after the activation treatment in 10 mM CuSO_4 for 20 min as shown in Figure 6 (note the imaged

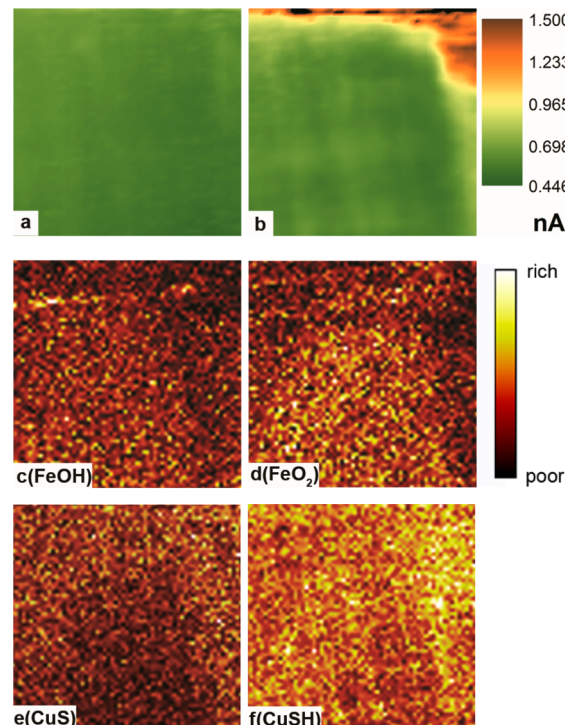


Figure 6. SECM images ($100 \times 100 \mu\text{m}^2$) of sphalerite (a) before and (b) after copper activation. The corresponding SIMS images of (c, d) Fe species and (e, f) Cu species at the same location after the SECM measurements.

region was fixed). From the SECM images, the nonuniform current increase can be seen in Figure 6b as compared to Figure 6a. It should be noted that a current increase can be observed at the top of Figure 6b, where a carved line was produced by scratching prior to the SECM experiments as a marker on the sphalerite surface to help locate the fixed region for conducting *in situ* measurements. Empirically, when the active spot radius $a_s > 16.3 \mu\text{m}$, the theoretical model shown in eqs 5–9 can be applied.³⁴ The size of carved region at the top right corner of the sphalerite surface (in Figure 6) is $>20 \mu\text{m}$. Therefore, it is

valid to apply the theoretical model to fit the PAC curve measured, and the results fit well with the theoretical curve with $k = 3.0 \times 10^{-2} \text{ cm s}^{-1}$ (blue triangles in Figure 3), which is close to the k value reported for Cu_xS .³⁶ Similar to the results in Figure 4, it is evident from Figure 6a and Figure 6b that the current response increase around the carved regions on the sphalerite surface after copper activation has to be due to the preferential adsorption of copper ions to form Cu_xS . Current change is also visible beyond the carved region as shown in Figure 6a and Figure 6b. From the SIMS results in Figure 6c–f, the regions with current increase correspond to CuS and CuSH (which is CuS associated with a hydrogen atom during the ion bombardment), while the areas with current decrease correspond to Fe oxide/hydroxide formed at Fe-rich regions as evident from the FeOH and FeO_2 fragments detected.

The valence states of surface species are further characterized by XPS spectra as shown in Figure 7. Before the copper

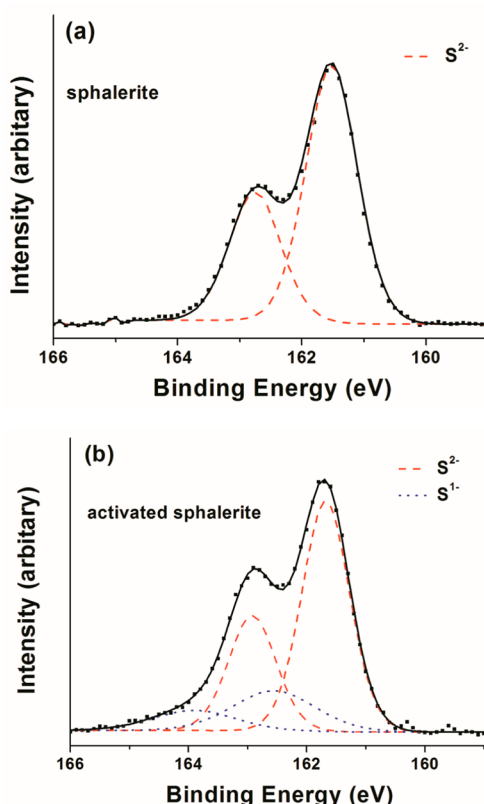


Figure 7. XPS spectra of S 2p of (a) unactivated and (b) activated sphalerite.

activation, only S^{2-} was detected on the surface as indicated by the S 2p doublet with its $\text{S} 2\text{p}_{3/2}$ at 161.5 eV (Figure 7a), which agrees with results from previous studies.⁶³ After the copper activation, two S 2p doublets were detected and further fitted at 161.6 and 162.5 eV of $\text{S} 2\text{p}_{3/2}$. The first doublet can be assigned as S^{2-} , which shifts from 161.5 eV of unactivated sphalerite to 161.6 eV of the activated one, indicating an increase of surface conductivity.¹⁴ The second doublet originates from the S^1- component, which is the product of coupled solid-state electrochemical process to form $\text{Cu(I)}\text{S}(-\text{I})$ through the oxidation of $\text{S}(-\text{II})$ to $\text{S}(-\text{I})$ and reduction of Cu(II) to Cu(I) .¹⁴ The charge shift in XPS spectra decreases from 2.6 eV of unactivated sphalerite to 0.5 eV of the activated one, which

also indicates an increase of surface conductivity. Both the XPS spectra and SIMS mapping indicate the presence of CuS-like species on the sphalerite surface after copper activation.

4. CONCLUSIONS

The copper activation and subsequent xanthate adsorption on sphalerite were investigated *in situ* using the SECM technique for the first time. Different from traditional electroanalytical techniques, SECM is suitable for the study of surfaces with low conductivity such as sphalerite. The probe approach curves in SECM measurements show that unactivated and activated sphalerite surfaces have negative current feedback and partially positive current feedback, respectively, implying the formation of Cu_xS on the surface. The SECM and ToF-SIMS results further revealed that the copper activation of sphalerite strongly depends on the surface heterogeneity such as the polishing defects and composition, which directly impacts the subsequent xanthate adsorption process. It is evident from the SECM, ToF-SIMS, and XPS analysis that during the copper activation, (1) the polishing defects tend to consume more copper ions, resulting in Cu-rich regions composed of CuS-like species, and (2) Fe oxide/hydroxide forms at Fe-rich regions with low current response. The XPS spectra confirm that the CuS-like species involve Cu(I) and S(-I). The SECM analysis shows that after xanthate adsorption, the current response at the Cu-rich regions decreases because of the formation of CuX and X_2 , while it increases at the Fe-rich regions mainly because of the chemisorbed xanthate on Fe oxide/hydroxide in a possible form of ferric hydroxyl xanthate $\text{Fe(OH)}_n(\text{X})_{3-n}$. This work provides new insights into the fundamental understanding of the electrochemical processes on sphalerite surface associated with its copper activation and subsequent xanthate adsorption in flotation. The methodology may be also applied to the *in situ* analysis of electrochemical processes of other sulfide minerals or surfaces with low conductivity.

■ ASSOCIATED CONTENT

■ Supporting Information

SECM images after subtracting the current response in Figure 4a from Figure 4b and after subtracting the current response in Figure 4b from Figure 4c. This material is available free of charge via the Internet at <http://pubs.acs.org>.

■ AUTHOR INFORMATION

Corresponding Author

*E-mail: hongbo.zeng@ualberta.ca. Phone: +1-780-492-1044. Fax: +1-780-492-2881.

Notes

The authors declare no competing financial interest.

■ ACKNOWLEDGMENTS

We gratefully acknowledge financial support from the Canadian Centre for Clean Coal/Carbon and Mineral Processing Technologies (C⁵MPT), the Natural Sciences and Engineering Research Council of Canada (NSERC), and the Canada Foundation for Innovation (CFI). We also thank Dr. Anqiang He (ACSES, University of Alberta, Canada) for the ToF-SIMS analysis.

■ REFERENCES

- (1) Bowen, P. K.; Drelich, J.; Goldman, J. Zinc Exhibits Ideal Physiological Corrosion Behavior for Bioabsorbable Stents. *Adv. Mater.* **2013**, *25*, 2577–2582.
- (2) Godfrey Alig, A. R.; Akbulut, M.; Golan, Y.; Israelachvili, J. Forces between Surfactant-Coated ZnS Nanoparticles in Dodecane: Effect of Water. *Adv. Funct. Mater.* **2006**, *16*, 2127–2134.
- (3) Jüstel, T.; Möller, S.; Winkler, H.; Adam, W. Luminescent Materials. In *Ullmann's Encyclopedia of Industrial Chemistry*; Wiley-VCH: Weinheim, Germany, 2000.
- (4) Auer, G.; Woditsch, P.; Westerhaus, A.; Kischkowitz, J.; Griebler, W.-D.; De Liedekerke, M. Pigments, Inorganic, 2. White Pigments. In *Ullmann's Encyclopedia of Industrial Chemistry*; Wiley-VCH: Weinheim, Germany, 2000.
- (5) Tao, D. Role of Bubble Size in Flotation of Coarse and Fine Particles—A Review. *Sep. Sci. Technol.* **2004**, *39*, 741–760.
- (6) Sutherland, K. L.; Wark, I. W. *Principles of Flotation*; Australasian Institute of Mining and Metallurgy: Melbourne, Australia, 1955.
- (7) Klassen, V. I.; Mokrousov, V. A. *An Introduction to the Theory of Flotation*; Butterworths: London, 1963.
- (8) Fuerstenau, M. C.; Miller, J. D.; Kuhn, M. C. *Chemistry of Flotation*; Society of Mining Engineers of the American Institute of Mining, Metallurgical and Petroleum Engineers: New York, 1985.
- (9) Buckley, A. N.; Woods, R.; Wouterlood, H. J. An XPS Investigation of The Surface of Natural Sphalerites under Flotation-Related Conditions. *Int. J. Miner. Process.* **1989**, *26*, 29–49.
- (10) Gigowski, B.; Vogg, A.; Wierer, K.; Dobias, B. Effect of Fe-Lattice Ions on Adsorption, Electrokinetic, Calorimetric and Flotation Properties of Sphalerite. *Int. J. Miner. Process.* **1991**, *33*, 103–120.
- (11) Fornasiero, D.; Ralston, J. Effect of Surface Oxide/Hydroxide Products on the Collectorless Flotation of Copper-Activated Sphalerite. *Int. J. Miner. Process.* **2006**, *78*, 231–237.
- (12) Popov, S. R.; Vučinić, D. R. The Ethylxanthate Adsorption on Copper-Activated Sphalerite under Flotation-Related Conditions in Alkaline Media. *Int. J. Miner. Process.* **1990**, *30*, 229–244.
- (13) Leppinen, J. O. FTIR and Flotation Investigation of the Adsorption of Ethyl Xanthate on Activated and Non-Activated Sulfide Minerals. *Int. J. Miner. Process.* **1990**, *30*, 245–263.
- (14) Kartio, I. J.; Basilio, C. I.; Yoon, R. H. An XPS Study of Sphalerite Activation by Copper. *Langmuir* **1998**, *14*, 5274–5278.
- (15) Lascelles, D.; Sui, C. C.; Finch, J. A.; Butler, I. S. Copper Ion Mobility in Sphalerite Activation. *Colloids Surf., A* **2001**, *186*, 163–172.
- (16) Chen, Z. Electrochemical Studies of Copper-Activation of Sphalerite and Pyrite. Ph.D. Thesis, Virginia Polytechnic Institute and State University, 1998.
- (17) Patrick, R. A. D.; England, K. E. R.; Charnock, J. M.; Mosselmans, J. F. W. Copper Activation of Sphalerite and Its Reaction with Xanthate in Relation to Flotation: An X-ray Absorption Spectroscopy (Reflection Extended X-ray Absorption Fine Structure) Investigation. *Int. J. Miner. Process.* **1999**, *55*, 247–265.
- (18) Boulton, A.; Fornasiero, D.; Ralston, J. Effect of Iron Content in Sphalerite on Flotation. *Miner. Eng.* **2005**, *18*, 1120–1122.
- (19) Harmer, S. L.; Mierczynska-Vasilev, A.; Beattie, D. A.; Shapter, J. G. The Effect of Bulk Iron Concentration and Heterogeneities on the Copper Activation of Sphalerite. *Miner. Eng.* **2008**, *21*, 1005–1012.
- (20) Chandra, A. P.; Gerson, A. R. A Review of The Fundamental Studies of the Copper Activation Mechanisms for Selective Flotation of the Sulfide Minerals, Sphalerite and Pyrite. *Adv. Colloid Interface Sci.* **2009**, *145*, 97–110.
- (21) Di Benedetto, F. Compositional Zoning in Sphalerite Crystals. *Am. Mineral.* **2005**, *90*, 1384–1392.
- (22) Stowe, K. G.; Chryssoulis, S. L.; Kim, J. Y. Mapping of Composition of Mineral Surfaces by TOF-SIMS. *Miner. Eng.* **1995**, *8*, 421–430.
- (23) Piantadosi, C.; Jasieniak, M.; Skinner, W. M.; Smart, R. S. C. Statistical Comparison of Surface Species in Flotation Concentrates and Tails from TOF-SIMS Evidence. *Miner. Eng.* **2000**, *13*, 1377–1394.
- (24) Piantadosi, C.; Smart, R. S. C. Statistical Comparison of Hydrophobic and Hydrophilic Species on Galena and Pyrite Particles in Flotation Concentrates and Tails from TOF-SIMS Evidence. *Int. J. Miner. Process.* **2002**, *64*, 43–54.
- (25) Peevler, J.; Fayek, M.; Misra, K. C.; Riciputi, L. R. Sulfur Isotope Microanalysis of Sphalerite by SIMS: Constraints on the Genesis of Mississippi Valley-Type Mineralization, from the Mascot-Jefferson City District, East Tennessee. *J. Geochem. Explor.* **2003**, *80*, 277–296.
- (26) Boulton, A.; Fornasiero, D.; Ralston, J. Characterisation of Sphalerite and Pyrite Flotation Samples by XPS and ToF-SIMS. *Int. J. Miner. Process.* **2003**, *70*, 205–219.
- (27) Khmeleva, T. N.; Georgiev, T. V.; Jasieniak, M.; Skinner, W. M.; Beattie, D. A. XPS and ToF-SIMS Study of a Chalcopyrite-Sphalerite Mixture Treated with Xanthate and Sodium Bisulphite. *Surf. Interface Anal.* **2005**, *37*, 699–709.
- (28) Verdier, S.; Metson, J. B.; Dunlop, H. M. Static SIMS Studies of the Oxides and Hydroxides of Aluminium. *J. Mass Spectrom.* **2007**, *42*, 11–9.
- (29) Kalegowda, Y.; Harmer, S. L. Chemometric and Multivariate Statistical Analysis of Time-of-Flight Secondary Ion Mass Spectrometry Spectra from Complex Cu–Fe Sulfides. *Anal. Chem.* **2012**, *84*, 2754–2760.
- (30) Wittmaack, K. Secondary Ion Mass Spectrometry as a Means of Surface Analysis. *Surf. Sci.* **1979**, *89*, 668–700.
- (31) Bard, A. J.; Fan, F. R. F.; Pierce, D. T.; Unwin, P. R.; Wipf, D. O.; Zhou, F. M. Chemical Imaging of Surfaces with the Scanning Electrochemical Microscope. *Science* **1991**, *254*, 68–74.
- (32) Bard, A. J.; Fan, F. R. F.; Kwak, J.; Lev, O. Scanning Electrochemical Microscopy. Introduction and Principles. *Anal. Chem.* **1989**, *61*, 132–138.
- (33) Kwak, J.; Bard, A. J. Scanning Electrochemical Microscopy. Apparatus and Two-Dimensional Scans of Conductive and Insulating Substrates. *Anal. Chem.* **1989**, *61*, 1794–1799.
- (34) Bard, A. J.; Mirkin, M. V.; Unwin, P. R.; Wipf, D. O. Scanning Electrochemical Microscopy. 12. Theory and Experiment of the Feedback Mode with Finite Heterogeneous Electron-Transfer Kinetics and Arbitrary Substrate Size. *J. Phys. Chem. C* **1992**, *96*, 1861–1868.
- (35) Wei, C.; Bard, A. J.; Mirkin, M. V. Scanning Electrochemical Microscopy. 31. Application of SECM to the Study of Charge Transfer Processes at the Liquid/Liquid Interface. *J. Phys. Chem. C* **1995**, *99*, 16033–16042.
- (36) Chen, M.; Zhao, J.; Zhao, X. Scanning Electrochemical Microscopy Studies of Micropatterned Copper Sulfide (Cu(x)S) Thin Films Fabricated by a Wet Chemistry Method. *Electrochim. Acta* **2011**, *56*, S016–S021.
- (37) Chen, Z.; Yoon, R.-H. Electrochemistry of Copper Activation of Sphalerite at pH 9.2. *Int. J. Miner. Process.* **2000**, *58*, 57–66.
- (38) Rao, S. R. *Xanthates and Related Compounds*; Marcel Dekker: New York, 1971.
- (39) Teng, F.; Liu, Q.; Zeng, H. In Situ Kinetic Study of Zinc Sulfide Activation Using a Quartz Crystal Microbalance with Dissipation (QCM-D). *J. Colloid Interface Sci.* **2012**, *368*, 512–20.
- (40) Unwin, P. R.; Bard, A. J. Scanning Electrochemical Microscopy. 9. Theory and Application of the Feedback Mode to the Measurement of Following Chemical Reaction Rates in Electrode Processes. *J. Phys. Chem. C* **1991**, *95*, 7814–7824.
- (41) Taggart, J. E. Polishing Technique for Geologic Samples. *Am. Mineral.* **1977**, *62*, 824–827.
- (42) Arca, M.; Bard, A. J.; Horrocks, B. R.; Richards, T. C.; Treichel, D. A. Advances in Scanning Electrochemical Microscopy. Plenary Lecture. *Analyst* **1994**, *119*, 719–726.
- (43) Velmurugan, J.; Sun, P.; Mirkin, M. V. Scanning Electrochemical Microscopy with Gold Nanotips: The Effect of Electrode Material on Electron Transfer Rates. *J. Phys. Chem. C* **2009**, *113*, 459–464.
- (44) Popov, S. R.; Vučinić, D. R. Floatability and Adsorption of Ethyl Xanthate on Copper-Activated Sphalerite in Weakly Acidic Medium. *Colloids Surf.* **1990**, *47*, 81–94.

- (45) McKibben, M. A.; Barnes, H. L. Oxidation of Pyrite in Low Temperature Acidic Solutions: Rate Laws and Surface Textures. *Geochim. Cosmochim. Acta* **1986**, *50*, 1509–1520.
- (46) Hyland, M. M.; Bancroft, G. M. Palladium Sorption and Reduction on Sulphide Mineral Surfaces: An XPS and AES Study. *Geochim. Cosmochim. Acta* **1990**, *54*, 117–130.
- (47) Bisschop, J.; Dysthe, D. K.; Putnis, C. V.; Jamtveit, B. In Situ AFM Study of the Dissolution and Recrystallization Behaviour of Polished and Stressed Calcite Surfaces. *Geochim. Cosmochim. Acta* **2006**, *70*, 1728–1738.
- (48) Ghorbani, Y.; Mainza, A. N.; Petersen, J.; Becker, M.; Franzidis, J. P.; Kalala, J. T. Investigation of Particles with High Crack Density Produced by HPGR and Its Effect on the Redistribution of the Particle Size Fraction in Heaps. *Miner. Eng.* **2013**, *43–44*, 44–51.
- (49) Mirnezami, M.; Hashemi, M. S.; Finch, J. A. Measurement of Conductivity of Sulphide Particles Dispersed in Water. *Can. Metall. Q.* **2003**, *42*, 271–276.
- (50) Mielczarski, J. A.; Mielczarski, E.; Cases, J. M. Influence of Chain Length on Adsorption of Xanthates on Chalcopyrite. *Int. J. Miner. Process.* **1998**, *52*, 215–231.
- (51) Wang, X.; Eric Forssberg, K. S.; Bolin, N. J. Thermodynamic Calculations on Iron-Containing Sulphide Mineral Flotation Systems, I. The Stability of Iron-Xanthates. *Int. J. Miner. Process.* **1989**, *27*, 1–19.
- (52) Fornasiero, D.; Ralston, J. Iron Hydroxide Complexes and Their Influence on the Interaction between Ethyl Xanthate and Pyrite. *J. Colloid Interface Sci.* **1992**, *151*, 225–235.
- (53) Khan, A.; Kelebek, S. Electrochemical Aspects of Pyrrhotite and Pentlandite in Relation to Their Flotation with Xanthate. Part-I: Cyclic Voltammetry and Rest Potential Measurements. *J. Appl. Electrochem.* **2004**, *34*, 849–856.
- (54) Woods, R.; Young, C. A.; Yoon, R. H. Ethyl Xanthate Chemisorption Isotherms and Eh-pH Diagrams for the Copper/Water/Xanthate and Chalcocite/Water/Xanthate Systems. *Int. J. Miner. Process.* **1990**, *30*, 17–33.
- (55) Wang, X. H.; Forssberg, K. S. E. The Solution Electrochemistry of Sulfide-Xanthate-Cyanide Systems in Sulfide Mineral Flotation. *Miner. Eng.* **1996**, *9*, 527–546.
- (56) Grujicic, D.; Petic, B. Iron Nucleation Mechanisms on Vitreous Carbon During Electrodeposition from Sulfate and Chloride Solutions. *Electrochim. Acta* **2005**, *50*, 4405–4418.
- (57) Drazic, D. M. *Modern Aspects of Electrochemistry*; Plenum Press: New York, 1989; Vol. 19.
- (58) Haupt, S.; Strehblow, H. H. Corrosion, Layer Formation, and Oxide Reduction of Passive Iron in Alkaline Solution: A Combined Electrochemical and Surface Analytical Study. *Langmuir* **1987**, *3*, 873–885.
- (59) Khaselev, O.; Sykes, J. M. In-Situ Electrochemical Scanning Tunneling Microscopy Studies on the Oxidation of Iron in Alkaline Solution. *Electrochim. Acta* **1997**, *42*, 2333–2337.
- (60) Casellato, U.; Comisso, N.; Mengoli, G. Effect of Li Ions on Reduction of Fe Oxides in Aqueous Alkaline Medium. *Electrochim. Acta* **2006**, *51*, 5669–5681.
- (61) Wang, J.; Diao, P. Direct Electrochemical Detection of Pyruvic Acid by Cobalt Oxyhydroxide Modified Indium Tin Oxide Electrodes. *Electrochim. Acta* **2011**, *56*, 10159–10165.
- (62) Li, W. Z.; Qin, W. Q.; Sun, W.; Qiu, G. Z. Electrodeposition of Dixanthogen(TETD) on Pyrite Surface. *Trans. Nonferrous Met. Soc. China* **2007**, *17*, 154–158.
- (63) Dake, L. S.; Baer, D. R.; Zachara, J. M. Auger Parameter Measurements of Zinc Compounds Relevant to Zinc Transport in the Environment. *Surf. Interface Anal.* **1989**, *14*, 71–75.